

.....
Structure of the ESCRT-II endosomal trafficking complex

Aitor Hierro¹, Ji Sun², Alexander S. Rusnak², Jaewon Kim¹, Gali Prag¹, Scott D. Emr² & James H. Hurley¹

¹Laboratory of Molecular Biology, National Institute of Diabetes and Digestive and Kidney Diseases, National Institutes of Health, US Department of Health and Human Services, Bethesda, Maryland 20892-0580, USA

²Department of Cellular and Molecular Medicine and Department of Chemistry and Biochemistry and Howard Hughes Medical Institute, University of California at San Diego, 9500 Gilman Drive, La Jolla, California 92093-0668, USA

The multivesicular-body (MVB) pathway delivers transmembrane proteins and lipids to the lumen of the endosome. The multivesicular-body sorting pathway has crucial roles in growth-factor-receptor downregulation¹, developmental signalling²⁻⁴, regulation of the immune response⁵ and the budding of certain enveloped viruses such as human immunodeficiency virus⁶. Ubiquitination is a signal for sorting into the MVB pathway^{7,8}, which also requires the functions of three protein complexes, termed ESCRT-I, -II and -III (endosomal sorting complex required for transport)^{7,9,10}. Here we report the crystal structure of the core of the yeast ESCRT-II complex, which contains one molecule of the Vps protein Vps22, the carboxy-terminal domain of Vps36 and two molecules of Vps25, and has the shape of a capital letter 'Y'. The amino-terminal coiled coil of Vps22 and the flexible linker leading to the ubiquitin-binding NZF domain of Vps36 both protrude from the tip of one branch of the 'Y'. Vps22 and Vps36 form nearly equivalent interactions with the two Vps25 molecules at the centre of the 'Y'. The structure suggests how ubiquitinated cargo could be passed between ESCRT components of the MVB pathway through the sequential transfer of ubiquitinated cargo from one complex to the next.

The MVB pathway delivers transmembrane proteins and lipids into small vesicles that invaginate into the lumen of the endosome. MVBs then fuse with the vacuole/lysosome and release the vesicles into the lumen where they are degraded by the hydrolases contained in the vacuole/lysosome¹. Proteins that remain in the limiting membrane of the MVB are either delivered to the lysosomal/vacuolar limiting membrane or they are recycled to the Golgi complex or the plasma membrane. Therefore, the MVB sorting pathway plays a critical role in the trafficking of numerous cargo proteins within the endosomal membrane system.

Sorting of proteins into the MVB pathway is a complex, multi-step process. It requires coordinated functions of many protein complexes that are conserved from yeast to humans. Screens in *Saccharomyces cerevisiae* have identified numerous genes required for the sorting and trafficking of proteins into the MVB. Mutations in these genes result in defects in the sorting of transmembrane proteins, such as the G-protein-coupled receptor, Ste2p, from the plasma membrane to the vacuolar lumen by means of the MVB pathway. Thus far, more than 20 genes referred to as class E VPS (vesicular protein sorting) genes have been identified^{11,12}.

During MVB sorting, Hrs-Vps27 is first recruited to the early endosome by virtue of its FYVE domain interaction with PI(3)P (refs 13-15) and its UIM (ubiquitin interacting motif) interaction with ubiquitinated cargo. It then recruits the ESCRT-I complex (composed of Vps23, 28, 37) to the membrane¹⁶. ESCRT-I recruits the downstream ESCRT-II and ESCRT-III complexes⁹. After the ESCRTs have been recruited to the endosome membrane, the AAA-type ATPase Vps4 binds ESCRT-III and following MVB vesicle formation catalyses the dissociation of the ESCRT protein complexes in an ATP-dependent manner for further rounds of protein sorting¹⁷. The MVB sorting process is topologically equivalent to the

(Protein Data Bank entry 1L3S as the probe) and models refined using CNS²⁶. CNS topology and parameter files for 8oxoG refinement were generated with PRODRG²⁷. Structures were superimposed using the C α atoms of the palm subdomain (residues 646-655, 823-838, 863-869).

Received 28 May; accepted 2 August 2004; doi:10.1038/nature02908.
 Published online 22 August 2004.

1. Lindahl, T. Instability and decay of the primary structure of DNA. *Nature* **362**, 709-715 (1993).
2. Finkel, T. & Holbrook, N. J. Oxidants, oxidative stress and the biology of ageing. *Nature* **408**, 239-247 (2000).
3. Shibutani, S., Takeshita, M. & Grollman, A. P. Insertion of specific bases during DNA synthesis past the oxidation-damaged base 8-oxodG. *Nature* **349**, 431-434 (1991).
4. Greenblatt, M. S., Bennett, W. P., Hollstein, M. & Harris, C. C. Mutations in the p53 tumor suppressor gene: clues to cancer etiology and molecular pathogenesis. *Cancer Res.* **54**, 4855-4878 (1994).
5. Hainaut, P. et al. IARC Database of p53 gene mutations in human tumors and cell lines: updated compilation, revised formats and new visualisation tools. *Nucleic Acids Res.* **26**, 205-213 (1998).
6. Lowe, L. G. & Guengerich, F. P. Steady-state and pre-steady-state kinetic analysis of dNTP insertion opposite 8-oxo-7,8-dihydroguanine by *Escherichia coli* polymerases I exo- and II exo. *Biochemistry* **35**, 9840-9849 (1996).
7. Furge, L. L. & Guengerich, F. P. Analysis of nucleotide insertion and extension at 8-oxo-7,8-dihydroguanine by replicative T7 polymerase exo- and human immunodeficiency virus-1 reverse transcriptase using steady-state and pre-steady-state kinetics. *Biochemistry* **36**, 6475-6487 (1997).
8. Freisinger, E., Grollman, A. P., Miller, H. & Kisker, C. Lesion (in)tolerance reveals insights into DNA replication fidelity. *EMBO J.* **23**, 1494-1505 (2004).
9. Johnson, S. J., Taylor, J. S. & Beese, L. S. Processive DNA synthesis observed in a polymerase crystal suggests a mechanism for the prevention of frameshift mutations. *Proc. Natl Acad. Sci. USA* **100**, 3895-3900 (2003).
10. Johnson, S. J. & Beese, L. S. Structures of mismatch replication errors observed in a DNA polymerase. *Cell* **116**, 803-816 (2004).
11. Kiefer, J. R., Mao, C., Braman, J. C. & Beese, L. S. Visualizing DNA replication in a catalytically active *Bacillus* DNA polymerase crystal. *Nature* **391**, 304-307 (1998).
12. Goodman, M. F. Hydrogen bonding revisited: geometric selection as a principal determinant of DNA replication fidelity. *Proc. Natl Acad. Sci. USA* **94**, 10493-10495 (1997).
13. Kool, E. T. Active site tightness and substrate fit in DNA replication. *Annu. Rev. Biochem.* **71**, 191-219 (2002).
14. Miller, H. & Grollman, A. P. Kinetics of DNA polymerase I (Klenow fragment exo-) activity on damaged DNA templates: effect of proximal and distal template damage on DNA synthesis. *Biochemistry* **36**, 15336-15342 (1997).
15. Krahn, J. M., Beard, W. A., Miller, H., Grollman, A. P. & Wilson, S. H. Structure of DNA polymerase beta with the mutagenic DNA lesion 8-oxodeoxyguanine reveals structural insights into its coding potential. *Structure (Camb.)* **11**, 121-127 (2003).
16. Echols, H. & Goodman, M. F. Fidelity mechanisms in DNA replication. *Annu. Rev. Biochem.* **60**, 477-511 (1991).
17. Goodman, M. F., Creighton, S., Bloom, L. B. & Petruska, J. Biochemical basis of DNA replication fidelity. *Crit. Rev. Biochem. Mol. Biol.* **28**, 83-126 (1993).
18. Kunkel, T. A. & Bebenek, K. DNA replication fidelity. *Annu. Rev. Biochem.* **69**, 497-529 (2000).
19. Nair, D. T., Johnson, R. E., Prakash, S., Prakash, L. & Aggarwal, A. K. Replication by human DNA polymerase- α occurs by Hoogsteen base-pairing. *Nature* **430**, 377-380 (2004).
20. Ling, H., Boudsocq, F., Plosky, B. S., Woodgate, R. & Yang, W. Replication of a cis-syn thymine dimer at atomic resolution. *Nature* **424**, 1083-1087 (2003).
21. Culp, S. J., Cho, B. P., Kadlubar, F. F. & Evans, F. E. Structural and conformational analyses of 8-hydroxy-2'-deoxyguanosine. *Chem. Res. Toxicol.* **2**, 416-422 (1989).
22. Kouckadjian, M. et al. NMR structural studies of the ionizing radiation adduct 7-hydro-8-oxodeoxyguanosine (8-oxo-7H-dG) opposite deoxyadenosine in a DNA duplex. 8-Oxo-7H-dG(syn).dA(anti) alignment at lesion site. *Biochemistry* **30**, 1403-1412 (1991).
23. Kiefer, J. R. et al. Crystal structure of a thermostable *Bacillus* DNA polymerase I large fragment at 2.1 Å resolution. *Structure* **5**, 95-108 (1997).
24. Boosalis, M. S., Petruska, J. & Goodman, M. F. DNA polymerase insertion fidelity. Gel assay for site-specific kinetics. *J. Biol. Chem.* **262**, 14689-14696 (1987).
25. Otwinowski, Z. & Minor, W. *Methods in Enzymology, Macromolecular Crystallography (Part A): Processing of X-ray Diffraction Data Collected in Oscillation Mode* (Academic Press, New York, 1997).
26. Brünger, A. T. et al. Crystallography & NMR system: A new software suite for macromolecular structure determination. *Acta Crystallogr. D* **54**, 905-921 (1998).
27. van Aalten, D. M. et al. PRODRG, a program for generating molecular topologies and unique molecular descriptors from coordinates of small molecules. *J. Comput. Aided Mol. Des.* **10**, 255-262 (1996).

Supplementary Information accompanies the paper on www.nature.com/nature.

Acknowledgements We thank H. W. Hellinga for critical reading of the manuscript. Research was carried out in part at the SER-CAT 22-ID beamline at the Advanced Photon Source (Argonne National Laboratory), which is supported by the US Department of Energy, Office of Energy Research. We also thank J. J. Warren for assistance with data collection. The work was supported by grants to L.S.B. from the National Cancer Institute and the Duke Comprehensive Cancer Center, and to T.C. from the Deutsche Forschungsgemeinschaft, the Volkswagen Stiftung and the Fonds of the German Chemical Industry. M.O. is supported by a fellowship from the Boehringer Ingelheim Foundation.

Competing interests statement The authors declare that they have no competing financial interests.

Correspondence and requests for materials should be addressed to L.S.B. (lsb@biochem.duke.edu). Coordinates have been deposited in the Protein Data Bank under accession codes 1U45, 1U47, 1U48, 1U49 and 1U4B.

budding process for envelope viruses such as human immunodeficiency virus (HIV), equine infectious anaemia virus (EIAV) and Ebola, suggesting a potential role for the ESCRTs in this event. In fact, it has been shown that TSG101–Vps23p binds to the p6 domain of HIV-1 Gag protein and inhibition of this binding inhibits viral budding⁶. The same inhibitory effect is seen with dominant negative SKD1, the mammalian Vps4 orthologue⁶.

Here we report the 3.6 Å resolution structure of the quaternary ESCRT-II complex containing Vps22, Vps36 and two Vps25 molecules. Apart from the two NZF domains of Vps36, nothing is known about the structures of any of the ESCRT subunits alone or in the complex. These structures, in conjunction with mutational analyses, provide a framework for an initial understanding of the mechanisms for ESCRT assembly and function.

The 3.6 Å crystal structure of the ESCRT-II core complex (Supplementary Table 1 and Fig. 1a) contains two molecules of Vps25, one molecule of Vps22 and one copy of the C-terminal 171 amino acid residues of Vps36. The observed stoichiometry of 1 Vps22: 2 Vps25: 1 Vps36 leads to a calculated molecular weight of 138 kDa for the intact complex. This is consistent with the 155 kDa estimated on the basis of size exclusion chromatography of ESCRT-II purified from yeast⁹. The complex adopts the shape of a capital letter 'Y', with overall dimensions of 120 × 85 × 52 Å (Fig. 1b). The base of the 'Y' consists of one of the two molecules of Vps25; one of the branches of the 'Y' consists of the second molecule of Vps25, and the other branch is formed by a subcomplex consisting of Vps22 and the C-terminal domain of Vps36. The N terminus of Vps22 is a single α-helix that protrudes away from the tip of the 'Y' shape.

Vps22 consists of a single N-terminal coiled coil followed by two winged-helix (WH) domains (Supplementary Fig. 1a). All but the first 19 residues are ordered. The N-terminal domain consists of helices H2–H4, the C-terminal half of H1 and the N-terminal half of H5. Helix H5 is shared between the helical domain and the first WH domain. WH domains take the form HSHHSWSW, where H denotes a helix, S a β-strand and W a "wing"¹⁸, a loop inserted between or after the latter two of the three β-strands. Thus WH1 of Vps22 consists of H5–H7 and S1–S3. Strands 1–3 form an anti-parallel β-sheet with strand order S1–S3–S2. A one-turn helix follows WH2 and immediately precedes the C terminus.

The first helix projects 45 Å away from the core and forms a dimeric coiled coil with a symmetry-related Vps22 molecule. The presence of a coiled coil in this region was anticipated on the basis of sequence analysis⁹. We do not observe dimerization of ESCRT-II complexes isolated from yeast⁹ or in solution (not shown), and ESCRT-II dimerization is therefore unlikely to be the normal function of the Vps22 coiled coil. All of the ESCRT-III subunits

contain predicted coiled coils. On the basis of predictions from sequence analysis, it was proposed that an interaction occurs between a Vps22 coiled coil and coiled coils in the ESCRT-III subunits⁹.

Vps25 is the most flexible of the three subunits. Flexible internal loops between residues 56–70, 110–115, 146–149 and 162–164, as well as the C-terminal ten residues, could not be visualized in electron density. The N terminus of Vps25 consists of linked α- and 3₁₀-helical turns (Supplementary Fig. 1b). The diproline units Pro-5 and -6, and Pro-11 and -12, respectively, initiate the two α-helical turns. A modified WH motif follows immediately after the linked turns. The Vps25 WH1 is missing the middle helix, and contains four additional β-strands inserted in its place.

The Vps36 C-terminal domain consists of just two canonical WH domains (Supplementary Fig. 1c). There are short N- and C-terminal extensions and a short loop linking the two domains. Crystallization trials were initiated with a mixture of intact Vps22, Vps25 and Vps36. Upon microsequencing of redissolved crystals, it was determined that the crystallized complex contained a fragment of Vps36 comprising residues 396–566. The cleavage is attributed to trace amounts of protease contamination in the crystallized material. The proteolytic stability of the C-terminal portion of Vps36 is consistent with the structural finding that it makes extensive interactions within the core of the complex. The N-terminal portion of Vps36 contains two copies of a NZF zinc-finger motif. The second NZF finger of Vps36 binds ubiquitin and is thought to be the main site of interaction between ESCRT-II and ubiquitinated cargo proteins¹⁹. The proteolytic susceptibility of the region connecting the second NZF motif at residue 203 and the start of the C-terminal domain at 396 suggests that a flexible linker connects these two domains.

None of the three ESCRT-II subunits has discernable homology between each other at the amino acid sequence level. However all three have in common a structure based on two copies of the WH fold (Fig. 2a). For example, the WH2 of Vps36 superimposes on the WH2 of Vps22 with a root mean square deviation (r.m.s.d.) of 1.8 Å over 59 Cα positions (Fig. 2b). The internal WH folds also superimpose well on each other. The WH1 and WH2 folds of Vps22 can be superimposed with a r.m.s.d. of 1.9 Å for 51 Cα positions. In contrast to the similarity in the individual WH folds, the relative orientation of the two WH folds in Vps22 and Vps36 differ markedly, and the tandem WH fold cannot be superimposed simultaneously.

The Vps22–Vps36 interaction is the most extensive in the complex (Fig. 3a, b). This interaction buries a total of 2,527 Å² of solvent-accessible surface area from both partners, over a contact area whose longest dimension extends to 53 Å. The two subunits form a roughly parallel side-to-side arrangement, with the WH1

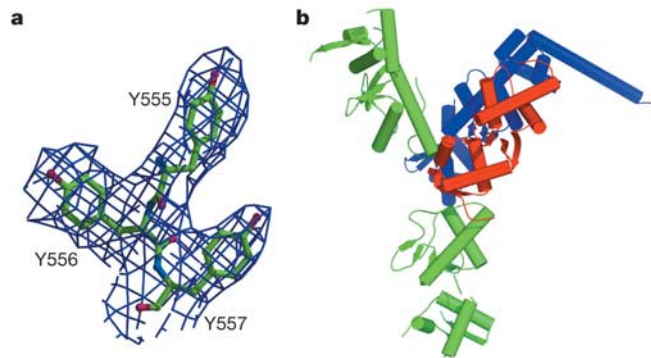


Figure 1 Structure of the ESCRT-II complex. **a**, Electron density from solvent-flattened SIRAS map contoured at 0.7 σ in the vicinity of the Vps25–Vps36 interface showing the refined structure in a stick model for Vps36 Tyr 555, Tyr 556 and Tyr 557. **b**, Overall structure of the complex: Vps22 is blue, Vps36 red and Vps25 green.

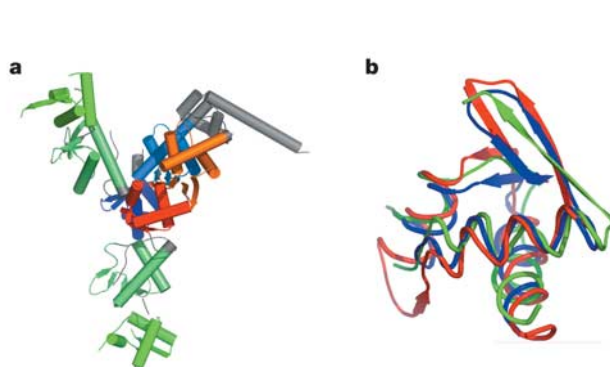


Figure 2 Winged helix folds in ESCRT-II. **a**, WH folds are highlighted in light and dark blue (Vps22 WH1 and WH2), light and dark green (Vps25 WH1 and WH2), and orange and red (Vps36 WH1 and WH2); the rest of the structure is coloured grey. **b**, Superposition of WH2 of Vps22, WH2 of Vps36 and WH2 of Vps25. Colours are as in Fig. 1.

and WH2 folds each in contact with their cognates from the opposing subunit.

Vps22 uses its C-terminal sheet and wings and adjacent regions to bind one Vps25 molecule (Fig. 3c). Vps25 interacts with Vps22 through its N terminus, helix H1 and the loop immediately preceding H3. The interaction buries a total of 1,689 Å² of solvent-accessible surface area from both partners. The focal point of the Vps25 binding site on Vps22 is an aromatic cage made up of the side chains of Trp 212, Trp 224 and Trp 228. Pro 226 and Ile 229 also contribute to the walls of the cage. Together these residues completely surround and bury Phe 10 of Vps25. The hydrophobic contact surface extends over a radius of roughly 10 Å surrounding Phe 10. In addition to the many hydrophobic interactions, a salt bridge is formed by the well-ordered side chains of Asp 214 (Vps22) and Arg 83 (Vps25). Vps22 approaches within 4 Å of Vps25 molecule 2, which is tightly bound to Vps36. Vps25 molecule 2 has little interaction with Vps22, burying a total of only 332 Å².

The parallels between the Vps36–Vps25 and Vps22–Vps25 interactions are striking (Fig. 3c–f). Phe 10 of Vps25 is buried in an aromatic cage on Vps36. The cage on the sheet and wings of Vps36 is formed by Leu 546, Tyr 557, Tyr 561 and Trp 562. A salt bridge is formed between Arg 83 of Vps25 and Asp 548 of Vps36. The total surface area buried is 1,524 Å², identical to that between Vps22 and Vps25, within error. In contrast to Vps22, Vps36 has significant interactions with the Vps25 molecule 1. This secondary interaction buries 736 Å² of surface area. Helix H5 and the hairpin turn between S5 and S6 of Vps36 make interactions with the N-terminal part of H1 of Vps25 molecule 1.

To determine which subunit interfaces participate in the assembly of ESCRT-II, and which interactions are required for function, mutations were engineered that blocked each of the subunit interfaces (Fig. 4). The Vps36 mutation Y441A disrupts hydrophobic

interactions between Vps36 and Leu 97, Ile 100, Leu 141 and Leu 144 of Vps22 (Fig. 3a). Vps36 Y441A has a class E phenotype, and forms a 1:1 Vps25:Vps36 subcomplex (Supplementary Table 2). The Vps22 mutation I100D disrupts the same hydrophobic cluster at Y441A (Fig. 3b). This mutant has a class E phenotype and forms a 1:1 Vps22:Vps25 subcomplex (Fig. 4a). The behaviour of these mutants shows that the Vps22–Vps36 interface is subject to mutational disruption, that subcomplexes can exist *in vivo* without this interface and that subcomplexes lacking Vps22 or Vps36 are not functional *in vivo*.

To analyse the functions of the two Vps25 molecules, mutations were made in Vps25 and in the binding sites for Vps25 on Vps22 and Vps36. The mutation F10D at the heart of the Vps25 interface with both of the other two subunits (Fig. 3c–f) leads to a class E phenotype and the detection of Vps25 as a monomer only. The mutation R83D, which removes salt bridges with Vps22 Asp 214 and Vps36 Asp 548 (Fig. 3c–f), also leads to a class E phenotype and a monomer Vps25 (Fig. 4a, b). Of the three mutations in the Vps22 binding site for Vps25, W212D, D214A and Q216A, the first two lead to class E phenotypes and formation of 1:1:1 Vps22:Vps25:Vps36 subcomplexes (Fig. 4a, b). The mutation at Gln 216, which is more solvent-exposed and appears to make weaker interactions than the other two residues mutated in this site, has a wild-type sorting phenotype and forms the wild-type 1:2:1 tetramer. The Vps36 mutation D548A is the structural counterpart of the Vps22 mutation D214A, but has a wild-type phenotype. Vps25 molecule 2, the partner for the Vps36 binding site, buries 250 Å² more in interactions with the Vps22–Vps36 subcomplex than does Vps25 molecule 1. The additional interaction area may make it more difficult to disrupt this interaction. The mutation D548R disrupts the interface to a greater degree than D548A, and results in a class E phenotype and a 1:1:1

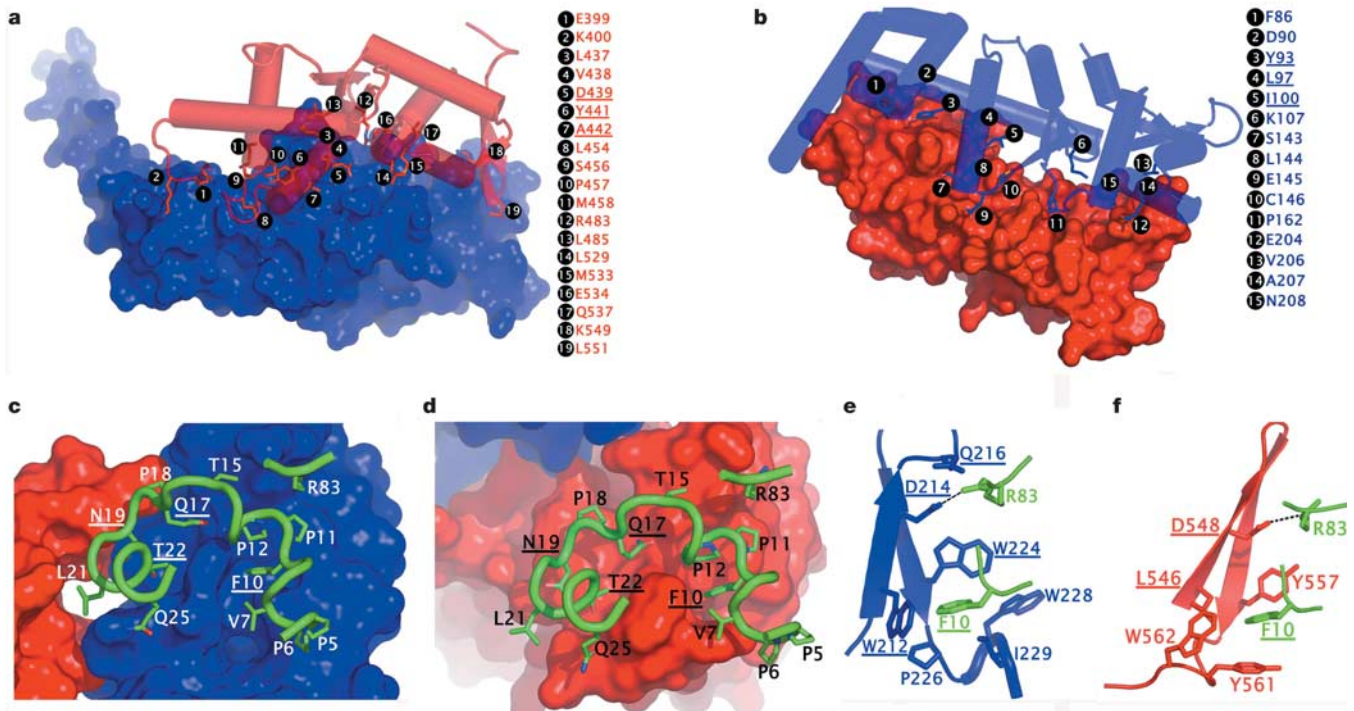


Figure 3 ESCRT-II complex assembly and subunit interactions. **a**, Vps22 (solid; blue) interactions with Vps36 (ribbons, cylinders and sticks; red). **b**, Vps36 (solid; red) interactions with Vps22 (ribbons, cylinders and sticks; blue). **c**, First Vps25 subunit (C-chain) N terminus (stick model; green) bound to surface of Vps22–Vps36 subcomplex (Vps22, blue; Vps36, red). **d**, Second Vps25 (D-chain) N terminus (stick model; green)

bound to subcomplex (surface Vps36, red; Vps22, blue). **e**, Wings and sheet of Vps22 (blue) interacting with Vps25 molecule 1 (green). **f**, Wings and sheets of Vps36 (red) interacting with Vps25 molecule 2 (green). Underlined residues were mutated as indicated in Supplementary Table 2.

Vps22:Vps25:Vps36 subcomplex (Fig. 4a). These results demonstrate that both Vps25 molecules are required for ESCRT-II complex assembly and sorting function.

The structure of the salt bridge between Arg 83 of Vps25 and Asp 548 of Vps36 suggested that a charge reversal mutation at one site might serve as a second-site suppressor of a mutation in the other site. The double mutant Vps25^{R83D} Vps36^{D548R} has a class E phenotype and a combination of Vps25 monomers at 1:1:1 Vps22:Vps25:Vps36 subcomplex is observed (Fig. 4a). The class E phenotype is consistent with the abrogation of the Vps22–Vps25 interface by the Vps25 R83D mutation, which is not rescued by the Vps36 D548R mutation. The existence of a 1:1:1 Vps22:Vps25:Vps36 subcomplex, as compared to its absence in

the R83D single mutant, is consistent with the rescue of the Vps25–Vps36 interface by the second mutation. This result elegantly corroborates the structural observation of charge complementarity in the Vps25 binding sites.

The study of the ESCRT-II complex reported here offers structural insight into the core complexes that sort ubiquitinated membrane proteins into multivesicular bodies. The central observations are that ESCRT-II consists of a rigid, Y-shaped core scaffold with a protruding coiled coil for putative interactions with other ESCRT complexes, and a ubiquitin-binding domain attached by a long flexible linker. The mechanism of ubiquitinated cargo sorting can now be considered in the context of three-dimensional structural information. This mechanism is operative in human cells and is of profound medical importance. The budding or fission of HIV-1 and other retroviruses from human macrophages, and under appropriate conditions other cell types, occurs by this pathway. Our report concerns the yeast ESCRT-II complex; the subunits of yeast ESCRT-II are highly homologous (Supplementary Fig. 2) with their human counterparts throughout the core (although the human homologue of Vps36 lacks the N-terminal NZF domains), and therefore the structure reported here provides a reasonable basis for insights into the sorting mechanism in both yeast and human cells.

At least three ubiquitin-binding domains are involved in three sequential steps in the recruitment and hand-off of ubiquitinated cargo between the Vps27–Hse1 (Hrs–STAM in mammals) and ESCRT complexes. The Vps27–Hse1 complex recruits ubiquitinated cargo through the UIMs in Vps27. The cargo is transferred to ESCRT-I where it is bound to by the UEV (ubiquitin conjugating enzyme E2 variant) domain of Vps23. The cargo is then transferred to the second NZF domain of Vps36 in ESCRT-II. The affinity of each of these domains for ubiquitin is modest: ~250, 500 and 180 μM for the Vps27 UIM-1^{20,21}, Vps23 UEV^{6,22,23} and Vps36 NZF-2¹⁹, respectively. Because the affinities are low and do not follow an obvious hierarchy, it is difficult to account for the specificity and directionality of trafficking on the basis of affinities alone.

The ESCRT-II structure shows that the coiled coil domain is closely juxtaposed with the Y-shaped core of the complex. This suggests that the larger oligomers of ESCRT complexes could form a highly organized scaffold. Such a scaffold could prevent the ubiquitinated cargo from diffusing away from one of the low-affinity binding domains in the complex. In contrast to the close juxtaposition of the coiled coil with the core, the ubiquitin-binding domain is attached to the core by a long tether. Whereas the structure of the ESCRT-I complex is unknown, the situation may be similar in that there is a predicted 40-amino-acid flexible linker between the ubiquitin-binding UEV domain of Vps23 and the remainder of the subunit. This suggests that these complexes are equipped with long swinging arms for the transfer of cargo over distances of tens to hundreds of Å in the course of sorting (Supplementary Fig. 3). A complete mechanistic understanding of this pathway will require additional structures of the remaining complexes as well as those of the higher order complexes of complexes. The resolution of the first one of these structures provides the first detailed glimpse into the mechanism of ESCRT complex formation and a conceptual and practical foundation for the long-term effort in the field to reach this goal. □

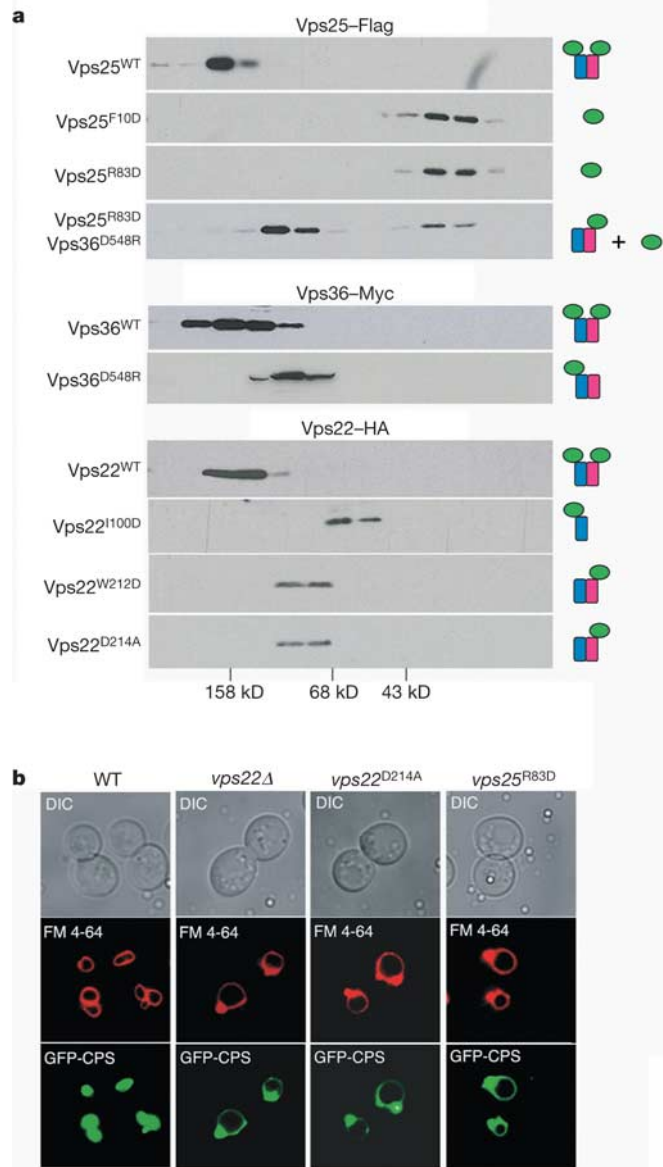


Figure 4 Mutational analysis of ESCRT-II subunit interfaces. **a**, Mutations at the molecular interface of ESCRT-II disrupt complex assembly, leading to subcomplex and monomer formation, as determined by gel filtration chromatography. Cartoons to the right (Vps25, green; Vps22, blue; and Vps36, red) indicate the corresponding complex/subcomplex composition of ESCRT-II and elution of molecular weight standards are indicated at the bottom. **b**, ESCRT-II subunit interface mutants exhibit defects in sorting MVB cargo (GFP–CPS) to the lumen of the vacuole and instead traffic them to the limiting membrane (FM4-64) of the vacuole.

Methods

Protein expression and purification

The DNA sequences encoding Vps22, Vps25 and Vps36 were amplified by polymerase chain reaction (PCR) to generate cassettes containing the Shine–Delgarno translational start signal and cloned directly into the polycistronic pST39 expression vector²⁴. Vps22 was tagged with an N-terminal hexahistidine tag and a TEV protease cleavage site; the other subunits were untagged. The plasmid was transformed into *Escherichia coli* strain BL21(DE3) Codon Plus RIL and expressed by inducing with 0.5 mM isopropylthiogalactoside (IPTG) at an absorbance at 600 nm (*A*₆₀₀) of 0.8 and grown at 15 °C for 36 h. Cells were lysed by high pressure homogenization in 50 mM Tris (pH 7.5), 300 mM NaCl, 5 mM β-mercaptoethanol (BME) and 100 μl of protease inhibitor cocktail

(Sigma) per litre of culture medium. The ESCRT-II complex was isolated using Talon Co²⁺ affinity chromatography (Clontech). The histidine tag was removed with TEV protease, concomitant with dialysis in 50 mM Tris (pH 8.0), 150 mM NaCl and 5 mM βME. The ESCRT-II complex was further purified with a second Talon affinity column and a Superdex S 200 gel filtration column.

Crystallization and data collection

Crystals of the ESCRT-II complex were obtained using hanging-drop vapour diffusion by mixing 3 μl of 10 mg ml⁻¹ protein solution and 3 μl of 100 mM HEPES (pH 7.4) and 1.4 M NaAcetate. Crystals grew to 0.7 mm per side in ~3 weeks. The content of the crystals was determined by mass spectrometry (MALDI-TOF) and automated N-terminal sequencing. Crystals were cryo-protected in mother liquor supplemented with 25% glycerol and flash-frozen in liquid nitrogen. Xenon-derivatized crystals were prepared in an Xcell pressure chamber (Oxford Cryosystems) at 20 bar for 5 min. Diffraction data were collected at λ = 1.0 Å from native and Xe-derivatized ESCRT-II crystals at beamline ID-22 at the Advanced Photon Source, using 0.5° oscillations, 1 s exposures and a Mar225 CCD (charge-coupled device) detector. Additional native data were collected at λ = 1.8 Å at beamline 9-2 at the Stanford Synchrotron Radiation Laboratory. Data were indexed and reduced using HKL2000 (HKL Research).

Structure determination

Five Xe sites were located in an automated Patterson search using the program SOLVE²⁵. The resulting density synthesis was improved by density modification in RESOLVE²⁶ using a solvent fraction of 0.75. The map was interpreted manually using the interactive graphics program O²⁷. Given the low resolution of the density map, the assignment of an amino acid sequence to the subunits was greatly facilitated by the use of secondary structure predictions²⁸. Subsequent to sequence assignment and model building, a λ = 1.8 Å native anomalous difference Fourier (ΔF) synthesis at 4.5 Å resolution was used to verify the locations of sulphur atoms in Cys and Met residues. The ΔF synthesis contained peaks for 8 of 11 S atoms in Vps22 (Met 36, Met 66 and Cys 67 absent), 9 of 9 S atoms in Vps36, and 3 of 3 S atoms in the N-terminal half of Vps25. The ΔF synthesis could not be interpreted reliably for the C-terminal half of Vps25 and the sequence assignment is therefore tentative for this region and for the N-terminal ~50 residues of Vps22. The model was refined in the CNS program using torsional dynamics and the maximum likelihood target function²⁹. The final model has no residues in disallowed regions of the Ramachandran plot.

Plasmid construction and yeast strains

DNA encoding a haemagglutinin (HA), Myc and Flag epitope were introduced just before the stop codon in the chromosomal copy of VPS22, VPS36 and VPS25, respectively. VPS22-HA, VPS36-Myc and VPS25-Flag sequences were then amplified from genomic DNA. The Sall/SpeI-digested PCR product of VPS22-HA, the SphI/SacII-digested PCR product of VPS36-Myc and the Sall/SacII-digested PCR product of VPS25-Flag were ligated with Sall/SpeI-digested pRS416, SphI/SacII-digested pSJ001 and Sall/SacII-digested pRS416, respectively, to generate pMB170, pSJ004 and pSJ072. Vps22, Vps36 and Vps25 interaction site mutations were introduced into pMB170, pSJ004 and pSJ072 by Quickchange mutagenesis (Stratagene). pGO45 (green fluorescent protein (GFP)-carboxypeptidase S (CPS) (GFP-CPS)) has been described³⁰. The following yeast strains were used: SEY6210 (MATα leu2-3, 112 ura3-52 his3-Δ200 trp1-Δ901lys2-801 suc2-Δ9); MBY31 (SEY6210.1; vps22Δ1::HIS3); MBY30 (SEY6210; vps36Δ1::HIS3)³¹; BWY101 (SEY6210; vps25Δ1::HIS3); SJY021 (SEY6210; vps25Δ1::HIS3 vps36Δ1::HIS3).

Microscopy

Living cells expressing the GFP-CPS chimera were harvested at an A₆₀₀ of 0.4–0.6, labelled with FM4-64 for vacuolar membrane staining and resuspended in medium for visualization. Visualization of cells was performed on a fluorescence microscope (Axiovert S1002TV; Carl Zeiss MicroImaging, Inc.) equipped with fluorescein isothiocyanate (FITC) and rhodamine filters, captured with a digital camera (Photometrix) and deconvolved using Delta Vision software (Applied Precision Inc.). Results presented were based on observations of >120 cells.

Gel filtration analysis

For gel filtration analysis, yeast cells were spheroplasted and lysed in PBS containing 0.1 mM AEBSEF, 1 μg ml⁻¹ pepstatin A, 1 μg ml⁻¹ leupeptin, 1 mM benzamide and protease inhibitor cocktail (Complete; Roche Molecular Biochemicals). The lysate was precleared for 5 min at 300 g followed by a 100,000 g centrifugation. The following lysate was loaded onto a Sephacryl S200 column (16/60; Amersham Life Sciences) and separated with PBS. Fractions were analysed with western blotting using anti-HA, anti-Myc and anti-Flag antibodies.

Received 13 July; accepted 9 August 2004; doi:10.1038/nature02914.
Published online 25 August 2004.

1. Futter, C. E., Pearse, A., Hewlett, L. J. & Hopkins, C. R. Multivesicular endosomes containing internalized EGF-EGF receptor complexes mature and then fuse directly with lysosomes. *J. Cell Biol.* **132**, 1011–1023 (1996).
2. Deldrande, G. A., Lai, E. C. & Kintner, C. *Xenopus* neuralized is a ubiquitin ligase that interacts with XDelta1 and regulates Notch signaling. *Dev. Cell* **1**, 795–806 (2001).

3. Lai, E. C., Deldrande, G. A., Kintner, C. & Rubin, G. M. *Drosophila* neuralized is a ubiquitin ligase that promotes the internalization and degradation of Delta. *Dev. Cell* **1**, 783–794 (2001).
4. Pavlopoulos, E. *et al.* neuralized encodes a peripheral membrane protein involved in Delta signaling and endocytosis. *Dev. Cell* **1**, 807–816 (2001).
5. Kleijmeier, M. *et al.* Reorganization of multivesicular bodies regulates MHC class II antigen presentation by dendritic cells. *J. Cell Biol.* **155**, 53–63 (2001).
6. Garrus, J. E. *et al.* Tsg101 and the vacuolar protein sorting pathway are essential for HIV-1 budding. *Cell* **107**, 55–65 (2001).
7. Katzmman, D. J., Babst, M. & Emr, S. D. Ubiquitin-dependent sorting into the multivesicular body pathway requires the function of a conserved endosomal protein sorting complex, ESCRT-I. *Cell* **106**, 145–155 (2001).
8. Reggiori, F. & Pelham, H. R. B. Sorting of proteins into multivesicular bodies: ubiquitin-dependent and -independent targeting. *EMBO J.* **20**, 5176–5186 (2001).
9. Babst, M., Katzmman, D. J., Snyder, W. B., Wendland, B. & Emr, S. D. Endosome-associated complex, ESCRT-II, recruits transport machinery for protein sorting at the multivesicular body. *Dev. Cell* **3**, 283–289 (2002).
10. Babst, M., Katzmman, D. J., Estepa-Sabal, E. J., Meerloo, T. & Emr, S. D. ESCRT-III: An endosome-associated heterooligomeric protein complex required for MVB sorting. *Dev. Cell* **3**, 271–282 (2002).
11. Raymond, C. K., Roberts, C. J., Moore, K. E., Howald, I. & Stevens, T. H. Biogenesis of the vacuole in *Saccharomyces cerevisiae*. *Int. Rev. Cytol.* **139**, 59–120 (1992).
12. Katzmman, D. J., Odorizzi, G. & Emr, S. D. Receptor downregulation and multivesicular-body sorting. *Nature Rev. Mol. Cell Biol.* **3**, 893–905 (2002).
13. Katzmman, D. J., Stefan, C. J., Babst, M. & Emr, S. D. Vps27 recruits ESCRT machinery to endosomes during MVB sorting. *J. Cell Biol.* **162**, 413–423 (2003).
14. Bache, K. G., Brech, A., Mehlum, A. & Stenmark, H. Hrs regulates multivesicular body formation via ESCRT recruitment to endosomes. *J. Cell Biol.* **162**, 435–442 (2003).
15. Bilodeau, P. S., Urbanowski, J. L., Winistorfer, S. C. & Piper, R. C. The Vps27p-Hse1p complex binds ubiquitin and mediates endosomal protein sorting. *Nature Cell Biol.* **4**, 534–539 (2002).
16. Lu, Q., Hope, L. W. Q., Brasch, M., Reinhard, C. & Cohen, S. N. TSG101 interaction with HRS mediates endosomal trafficking and receptor down-regulation. *Proc. Natl Acad. Sci. USA* **100**, 7626–7631 (2003).
17. Babst, M., Wendland, B., Estepa, E. J. & Emr, S. D. The Vps4p AAA ATPase regulates membrane association of a Vps protein complex required for normal endosome function. *EMBO J.* **17**, 2982–2993 (1998).
18. Gajiwala, K. S. & Burley, S. K. Winged helix proteins. *Curr. Opin. Struct. Biol.* **10**, 110–116 (2000).
19. Alam, S. L. *et al.* Ubiquitin interactions of NZF zinc fingers. *EMBO J.* **23**, 1411–1421 (2004).
20. Fisher, R. D. *et al.* Structure and ubiquitin binding of the ubiquitin-interacting motif. *J. Biol. Chem.* **278**, 28976–28984 (2003).
21. Swanson, K. A., Kang, R. S., Stamenova, S. D., Hicke, L. & Radhakrishnan, I. Solution structure of Vps27 UIM-ubiquitin complex important for endosomal sorting and receptor downregulation. *EMBO J.* **22**, 4597–4606 (2003).
22. Sundquist, W. I. *et al.* Ubiquitin recognition by the human TSG101 protein. *Mol. Cell* **13**, 783–789 (2004).
23. Teo, H., Veprincev, D. B. & Williams, R. L. Structural insights into ESCRT-I recognition of ubiquitinated proteins. *J. Biol. Chem.* in press.
24. Tan, S. A modular polycistronic expression system for overexpressing protein complexes in *Escherichia coli*. *Protein Expr. Purif.* **21**, 224–234 (2001).
25. Terwilliger, T. C. & Berendzen, J. Automated MAD and MIR structure solution. *Acta Crystallogr. D Biol. Crystallogr.* **55**, 849–861 (1999).
26. Terwilliger, T. C. Maximum-likelihood density modification. *Acta Crystallogr. D Biol. Crystallogr.* **56**, 965–972 (2000).
27. Jones, T. A., Zou, J. Y., Cowan, S. W. & Kjeldgaard, M. Improved methods for building protein models in electron-density maps and the location of errors in these models. *Acta Crystallogr. A* **47**, 110–119 (1991).
28. Rost, B. & Liu, J. F. The PredictProtein server. *Nucleic Acids Res.* **31**, 3300–3304 (2003).
29. Brunger, A. T. *et al.* Crystallography & NMR system: A new software suite for macromolecular structure determination. *Acta Crystallogr. D Biol. Crystallogr.* **54**, 905–921 (1998).
30. Odorizzi, G., Babst, M. & Emr, S. D. Fab1p PtdIns(3)P 5-kinase function essential for protein sorting in the multivesicular body. *Cell* **95**, 847–858 (1998).

Supplementary Information accompanies the paper on www.nature.com/nature.

Acknowledgements We thank P. P. di Fiore, M. Babst and B. Wendland for helpful discussions; M. Tabuchi for the Flag tag construct; and we acknowledge the use of the SER-CAT beamline at the APS, ANL and beamline 9-2 at the Stanford Synchrotron Radiation Laboratory. Use of the Advanced Photon Source was supported by the US Department of Energy, Basic Energy Sciences, Office of Science. The Stanford Synchrotron Radiation Laboratory, a national user facility operated by Stanford University on behalf of the US Department of Energy, is supported by the Department of Energy, Office of Biological and Environmental Research, and by the National Institutes of Health, National Center for Research Resources, Biomedical Technology Program and the National Institute of General Medical Sciences. S.D.E. is supported as an Investigator of the Howard Hughes Medical Institute.

Competing interests statement The authors declare that they have no competing financial interests.

Correspondence and requests for materials should be addressed to J.H.H. (hurley@helix.nih.gov). Coordinates have been deposited with the Protein Data Bank with accession number 1U5T.